Aerodynamic Modeling of Coaxial Counter-Rotating UAV Propellers

Moritz Thiele M.Sc. **Martin Obster** M.Sc. **Mirko Hornung** Prof. Dr.-Ing.
Institute of Aircraft Design – Technical University of Munich – Munich, Germany

ABSTRACT

While coaxial rotor systems experience complex aerodynamic effects, an application to eVTOL UAV can entail positive consequences for the overall system. Aerodynamic calculation of coaxial counter-rotating rotors is carried out and the knowledge gained is used to analyze a wingtip pusher propeller configuration. The aerodynamical model based on the BEMT is adapted to the use cases presented and includes azimuthal inflow and induced velocity components as well as the Prandtl tip loss factor. Wake contraction is calculated using an empirical model for the tip vortex. Moments acting on the rotor hub and oblique inflow can be considered by the discretization of the rotors at arbitrary azimuthal positions. Subsequently, the methods were validated against measurement data from literature and were found in good accordance. Based on aerodynamic parameters, the implemented methods and configurations can be used for rotor and propeller design and modifications.

NOTATION

Abbreviations

AoA	Angle of Attack	$[-]$
BEMT	Blade Element Momentum Theory	$[-]$
ESC	Electronic Speed Controller	$[-]$
eVTOL	electrical Vertical Take-Off and Landing	$[-]$
FVA	Free Vortex Analysis	$[-]$
MTOW	Maximum Take-Off Weight	$[-]$
SARF	Synthesis and Analysis Rotor Framework	$[-]$
UAV	Unmanned Aerial Vehicle	$[-]$

Letters

A	Rotor swept area	$[m^2]$
b	Wingspan	$[m]$
c	Sectional chord length	$[m]$
c_d	Sectional drag coefficient	$[-]$
c_l	Sectional lift coefficient	$[-]$
C_P	Rotor Power coefficient	$[-]$
c_P	Sectional Power coefficient	$[-]$
C_Q	Rotor Torque coefficient	$[-]$
C_T	Rotor Thrust coefficient	$[-]$
c_T	Sectional Thrust coefficient	$[-]$
D	Drag	$[N]$
F	Prandtl tip loss factor	$[-]$
FM	Figure of Merit	$[-]$
L	Lift	$[N]$
l	Sectional lift	$[N]$
$l1$	Lower rotor inner area	$[-]$
$l2$	Lower rotor outer area	$[-]$
N_b	Number of Blades	$[-]$
P	Power	$[W]$
R	Rotor tip radius	$[m]$
r	Radial coordinate	$[m]$
rpm	Revolutions per minute	$[\frac{1}{min}]$
rps	Revolutions per second	$[\frac{1}{s}]$
T	Thrust	$[N]$
t	Time	$[s]$
U	Velocity Component	$[\frac{m}{s}]$
V	Total Velocity	$[\frac{m}{s}]$
w	Induced velocity	$[\frac{m}{s}]$
x_{wing}	Distance wing leading edge to rotor disk	$[m]$

Greek Symbols

α	Angle of attack	$[rad]$
β	Blade or sectional pitch	$[rad]$
η	Propulsive efficiency	$[-]$
Γ	Circulation	$[\frac{m^2}{s}]$
λ_∞	Tip speed ratio	$[-]$
Ω	Rotational speed	$[\frac{rad}{s}]$
ϕ	Inflow angle	$[rad]$
Ψ_w	Wake angle	$[rad]$
ρ	Density of air	$[\frac{kg}{m^3}]$
σ	Rotor solidity	$[-]$
θ	Blade azimuth angle	$[rad]$
θ_b	Angle between two adjacent blades	$[rad]$
Θ_{lin}	Linear Blade Twist	$[rad]$

Indices

θ	Azimuthal direction	$[-]$
c	Contracted Wake	$[-]$
Hub	Rotor Hub	$[-]$
$Inflow$	Inflow on Rotor Disk	$[-]$
r	Radial direction	$[-]$
s	Wake Propagation	$[-]$
Tip	Rotor Tip	$[-]$
u/l	Upper / Lower rotor	$[-]$
wt	Wingtip	$[-]$
z	Axial direction	$[-]$

Presented at the 8th Biennial Autonomous VTOL Technical Meeting & 6th Annual Electric VTOL Symposium 2019, Mesa, Arizona, USA, Jan 29–31, 2019,

INTRODUCTION

The increasing use of civil and military eVTOL UAVs requires highly safe, reliable and efficient UAV configurations. Key components concerning UAV reliability are the motors used for hover propulsion. While inherently redundant electrical motors, possibly wired with 6 redundant phases, are still rare and heavy, a coaxial rotor system can enable higher redundancy while also maintaining a small areal footprint.

By providing sufficient lift in a small installation space this rotor arrangement may be used to reduce failure probabilities and meet safety requirements. Still, complex aerodynamic effects occur between the two rotors which consist of flow interaction and turbulent vortex structures.

Calculation of coaxial rotors has been the topic of several publications with most approaching the subject using a solver of the underlying Navier-Stokes equations as written by Ho (Ref. 1) and Barbely (Ref. 2). The theory used here is based on the model by Leishman and Ananthan (Ref. 3) for coaxial rotors in hover and axial flight. However, losses due to swirl and the effect on blade design as well as the influence of the lower rotor on the upper rotor are not incorporated in these calculations. This theory was used and improved to include the circumferential induced velocities proposed by Modarres and Peters (Ref. 4) as well as Giovanetti (Ref. 5). Those conclusions are adapted to calculate the local performance values at arbitrary azimuthal positions separately using the propeller calculation environment SARF, first described in (Ref. 6) and refined in (Ref. 7) to also consider oblique or arbitrary quasi stationary inflow. The goal was to use an underlying Blade Element Momentum Theory (BEMT) solution that differs from that proposed by Adkins and Liebeck (Ref. 8) which is already included in the SARF environment in also being valid while in hovering flight.

Validation for coaxial rotors relies mostly on the work of Harrington (Ref. 9) and Dingeldein (Ref. 10). Both use a full scale coaxial rotor in a wind-tunnel. Further validation of the method used here should also be carried out using the work of McAlister (Ref. 11) who used smaller rotors which are well suited for the intended purpose of designing VTOL UAV with this publication's calculations.

A major point of interest besides the calculation of classical coaxial rotor systems is the assessment of certain other configuration layouts which experience similar flow effects as the coaxial counter-rotating rotors.

For a eVTOL UAV to reach high endurance it is necessary to transition into a cruise flight state where the lift produced is supplied by wings as opposed to hover rotors on a multicopter. With electrical propulsion it is easy to mount a motor at the wing tip gaining an undisturbed flow over a very large part of the wing which increases efficiency. An exemplary concept for this kind of propulsion is the EVIATION "Orca" UAV. Additionally the wingtip propulsion can be used for yaw authority and thus eliminate the need for a separate rudder.

A wingtip mounted propeller can be used in a pusher or a tractor configuration. The pusher configuration promises to deliver some aerodynamic advantages where the propeller is operating in the wingtip vortex which positively influences the local inflow angle on the propeller blades. Additionally, by working against the wingtip vortex the propeller is actively reducing the wing's induced drag.

This alignment of the propeller and vortex present at the wingtip can be described similarly to a coaxial rotor and will be discussed below.

TECHNICAL APPROACH

The coaxial rotor system is described as two separate rotors operating in close proximity. The aerodynamic model is defined in a modular manner to enable a transfer of the model to configurations of equivalent modes of action like wingtip mounted pusher propellers.

Aerodynamic Modeling

Each rotor is modeled individually using a modified Blade Element Momentum Theory (BEMT) that includes additional azimuthal swirl components primarily following the approach developed by Giovanetti (Ref. 5). Subsequently the models of the two rotors are coupled while also considering the mutual interference effects and arbitrary inflow phenomena.

Blade Element Momentum Theory Following the classical BEMT approach each blade is discretized in a certain number of blade sections along the radius. These sections are described using the parameters shown in the upper half of figure 1. Additional information used for computation include the airfoil type and polars, chordlength and local blade sweep.

A rotor with rotational speed Ω is operating on a UAV in an arbitrary flight state. The inflow V_{Inflow} observed is examined in a local coordinate system turning with a rotor blade and can be written as the sum of three perpendicular components in axial (z), azimuthal (θ) and radial (r) directions. The magnitude and direction of V_{Inflow} is calculated using the functionality provided in SARF which was developed by Ost (Ref. 12).

$$V_{Inflow} = \sqrt{U_z^2 + U_\theta^2 + U_r^2} \tag{1}$$

The component in radial direction U_r is not considered for the BEMT but will be used for the calculation of oblique inflow phenomena.

To calculate the local sectional forces $\frac{dL}{dr}$ and $\frac{dD}{dr}$ the local relative inflow velocity V_{rel} has to be determined for each radial and azimuthal position according to the velocity vectors shown in the lower half of figure 1 by

$$V_{rel} = \sqrt{U_z^2 + (\Omega r + U_\theta)^2 - w^2} \tag{2}$$

This enables the calculation of the relative local flow angle ϕ:

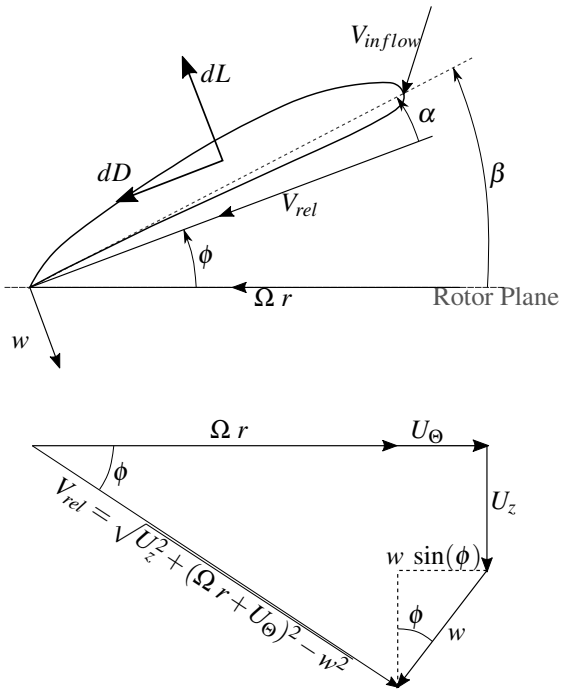

Fig. 1: Geometry of the flow at a blade section, including axial and swirl components of velocity

$$\sin\phi = \frac{U_z \cdot V_{rel} + w \cdot (\Omega r + U_\theta)}{U_z^2 + (\Omega r + U_\theta)^2} \tag{3}$$

$$\cos\phi = \frac{(\Omega r + U_\theta) \cdot V_{rel} - w \cdot U_z}{U_z^2 + (\Omega r + U_\theta)^2} \tag{4}$$

According to (Ref. 4) the sectional lift $\frac{dL}{dr}$ and profile drag $\frac{dD_{profile}}{dr}$ which are acting perpendicular and parallel to V_{rel} are obtained with a momentum balance.

$$\frac{dL}{dr} = 4\pi\rho F\ [U_z + w\cos\phi]\ w\ r \tag{5}$$

$$\frac{dD_{profile}}{dr} = \frac{1}{2}\rho N_b\ V_{rel}\ c\ c_d \tag{6}$$

The Prandtl Tip loss factor F is incorporated to consider tip losses.

By resolving this force in axial and azimuthal components and normalizing all velocities and lengths denoted with an overbar by $\Omega\ r_{Tip}$ and r_{Tip} respectively according to (Ref. 5), the equations of the non-dimensional local coefficients c_T and c_P are obtained. These have to be integrated in radial and azimuthal directions and lead to the thrust and power coefficients of the rotor C_T and C_P.

$$C_T = \int_0^{2\pi}\int_{\bar{r}_{Hub}}^{1} 4F\ (\bar{U}_z + \bar{w}\cos\phi)\ \bar{w}\cos\phi\ \bar{r}$$

$$-\sin\phi\ \frac{N_b\bar{c}c_d}{2\pi}\ \left(\bar{U}_z^2 + (\bar{r}+\bar{U}_\theta)^2 - \bar{w}^2\right)\ d\bar{r} \tag{7}$$

$$C_P = \int_0^{2\pi}\int_{\bar{r}_{Hub}}^{1} 4F\ (\bar{U}_z + \bar{w}\cos\phi)\ \bar{w}\sin\phi\ \bar{r}\ (\bar{r}+\bar{U}_\theta)$$

$$+\cos\phi\ \frac{N_b\bar{c}c_d}{2\pi}\ \left(\bar{U}_z^2 + (\bar{r}+\bar{U}_\theta)^2 - \bar{w}^2\right)\ (\bar{r}+\bar{U}_\theta)\ d\bar{r}\ . \tag{8}$$

In order to assess the rotor performance it is necessary to measure the efficiency. While this model is valid for the hovering as well as an axial or forward flight state, it is important to distinguish between those flight states when assessing the propulsive efficiency.

When operating in hover, the Figure of Merit (FM) is an adequate efficiency metric, however it is not valid in axial or forward flight ($U_\infty \neq 0$) and can only be used for the comparison of rotors with a similar disk loading (DL). It is defined, while hovering, as the ideal power required divided by the actual power required and can be calculated with:

$$FM = \frac{C_T^{3/2}}{2C_P} \tag{9}$$

For axial and forward flight the propulsive efficiency is given by

$$\eta = \frac{TU_\infty}{TU_\infty + P_i + P_0}\ . \tag{10}$$

The thrust T and power $P = P_i + P_0$ as the sum of profile power and induced power are defined based on the non dimensional coefficients:

$$T = C_T\rho A\Omega^2 r_{Tip}^2 \tag{11}$$

$$P = C_P\rho A\Omega^3 r_{Tip}^3 \tag{12}$$

Calculation of the Induced Velocity A remaining variable for the calculation is the induced velocity w. The induced velocity is produced by the lift of the rotor blades and is aligned in the opposite direction of the lift vector.

The base for the model used here is the BEMT where one key characteristic is the assumption that all radial annuli are independent and do not influence each other. From this the induced velocity at each blade section can be calculated by relating it to the local lift coefficient produced by the rotor. Depending on the relation between the rotational speed, the axial and the oblique inflow, it is possible for certain sections to produce a negative lift at certain azimuthal positions which has to be considered when calculating the total thrust and torque produced by the rotor.

The Blade Element Theory yields an expression for the normalized lift produced at each blade section:

$$\frac{d\bar{L}}{d\bar{r}} = \left(\frac{N_b\rho\bar{c}c_l}{2}\right)\ \left(\bar{r}^2 + \bar{U}_z^2 - \bar{w}^2\right)\ . \tag{13}$$

This can be extended to also consider azimuthal velocities U_θ and connected with the normalized equation (5) to:

$$\begin{aligned} 4\pi\rho F\ \left[\bar{U}_z + \bar{w}\cos\phi\right]\ \bar{w}\ r = \\ = \left(\frac{N_b \rho \bar{c} c_l}{2}\right)\ \left((\bar{r}+\bar{U}_\theta)^2 + \bar{U}_z^2 - \bar{w}^2\right) \end{aligned} \tag{14}$$

This quadratic equation of the induced velocity can be solved using the standard approach:

$$\bar{w}_{1,(2)} = \frac{-b \pm \sqrt{b^2 - 4ac}}{2a} \tag{15}$$

with the parameters a,b and c being:

$$\begin{aligned} a &= 8F\pi\bar{r}\cos\phi + \bar{c}N_b c_l \\ b &= 8F\pi\bar{r}\bar{U}_z \\ c &= -\bar{c}N_b c_l\left((\bar{r}+\bar{U}_\theta)^2 + \bar{U}_z^2\right) \end{aligned} \tag{16}$$

The positive solution of equation (15) results in the induced velocity of a rotor for a given inflow angle ϕ and local lift coefficient c_l. The induced velocity will be negative and thus pointed upward where negative lift is produced on the blade. As the local inflow angle ϕ, the resulting AoA α and the local lift coefficient c_l are themselves dependent of the induced velocity an iterative approach is used to solve the system for each rotor with a start value of the induced velocity that is required.

This start value is calculated based on the model proposed by Betz (Ref. 13) which describes the optimum inflow distribution for a maximum efficiency propeller. From this inflow distribution on an ideal rotor the postulated normalized induced velocity distribution over the blade can be extracted to be:

$$\bar{w}(r) = \frac{w(r)}{\Omega r_{Tip}} = \bar{w}_0\ cos(\phi) \tag{17}$$

with $\bar{w}_0 = \frac{w_0}{\Omega\ r_{Tip}}$ being a normalized nominal induced inflow velocity corresponding to an infinite rotor radius.

Relating the induced velocity to the inflow of the optimal rotor yields:

$$\bar{w}(r) = \frac{\bar{w}_0 r}{\sqrt{(\bar{V}_{rel} + \bar{w}_0)^2 + r^2}}\ . \tag{18}$$

To get an appropriate sectional start value for $\bar{w}(r)$ a constant value $\bar{w}_0 = 0.07$ for an optimal rotor in static conditions (hover) is taken from literature (Ref. 4). As this value is merely used to calculate the start value of $\bar{w}(r)$, it is also used for a non hovering operational state.

An iterative process for the calculation of rotor performance values can be set up for the given geometry of a rotor and its external inflow and is shown in the flowchart depicted in figure 2.

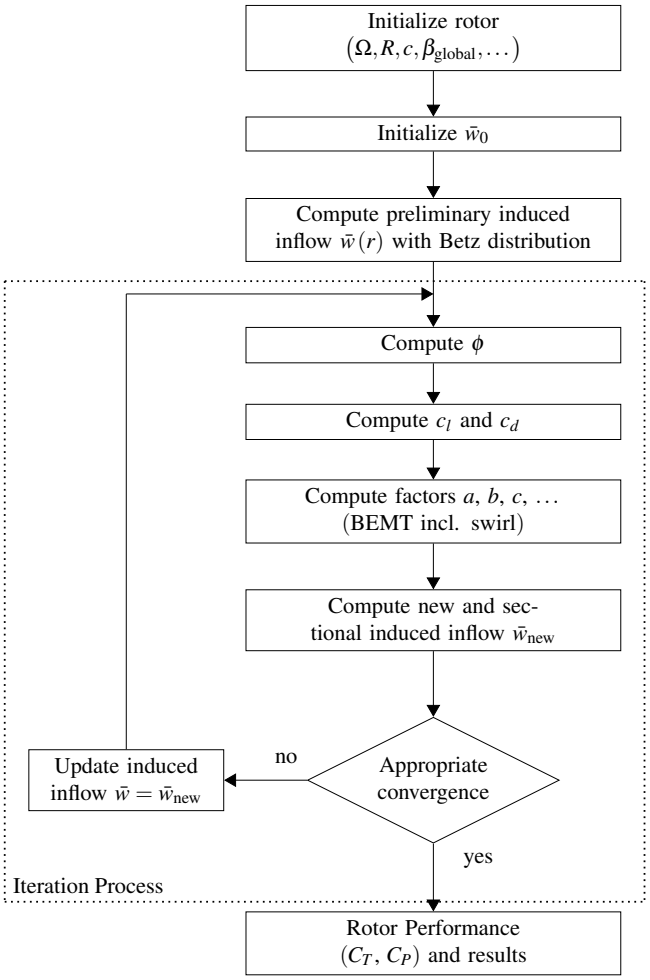

Fig. 2: Iterative process for the calculation of a single rotor

After the initialization of the rotor operating on a UAV an initial $\bar{w}_0$ is chosen to calculate $\bar{w}(r)$ using the Betz distribution. In the following iterative process the airfoil coefficients c_l and c_d are calculated for the local AoA α which depends on the inflow angle ϕ which is calculated in equation (3) and (4) considering all inflow velocities including the induced velocity. The resulting induced velocity $\bar{w}(r)$ can be determined with these coefficients and can be compared to the previous value until appropriate convergence is acquired. During this iteration process the Prandtl tip loss factor F is neglected to prevent an overshoot of the induced velocity of the outermost sections. It is again included in the calculation when the rotor performance values C_T and C_P are being determined using equations (7) and (8).

This model for a single rotor in an arbitrary flight state is then adapted to a coaxial rotor system.

Application to the Coaxial Rotor System A coaxial rotor system as shown in the schematic figure 3 is characterized by two distinct rotors separated by the distance z_{ul} in axial direction. When modeling this system the mutual influence of the two rotors has to be considered. The lower rotor (denoted by the subscript l) is operating in part in the slipstream of the upper rotor (subscript u).

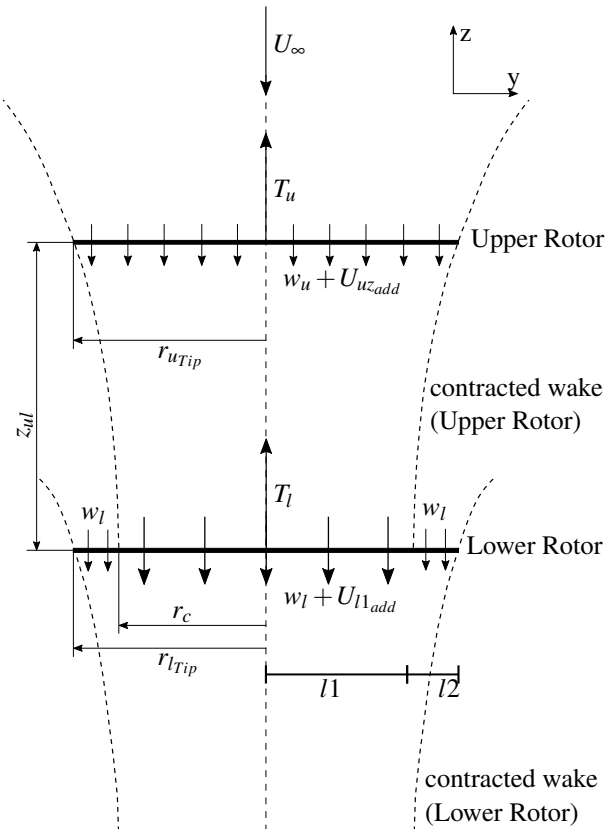

Fig. 3: Schematic of a coaxial rotor system with acting velocities

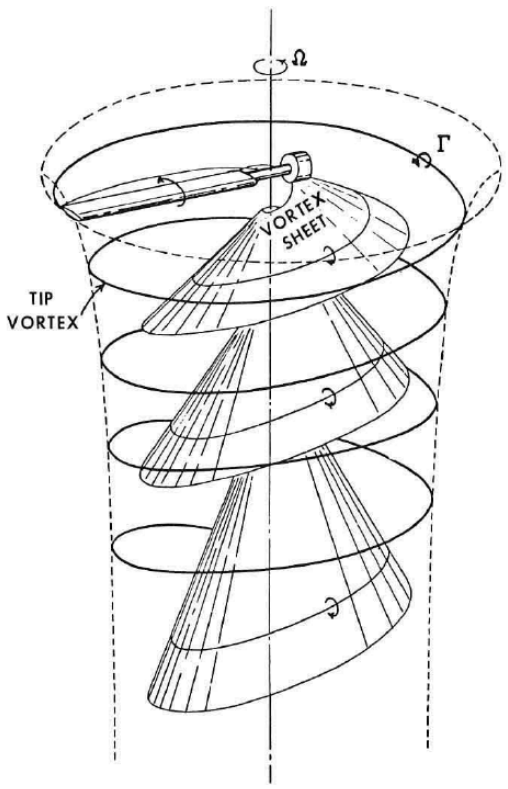

Fig. 4: Schematic rotor wake structure (Ref. 14)

The upper rotor is experiencing an additional induced flow velocity $\bar{U}_{uz_{add}}$ due to its location in the induced inflow velocity field of the lower rotor. This velocity is only considered in axial direction following a model by McAllister (Ref. 11) which is based on the Biot-Savart Law. It is generated by a helical vortex ring originating at the tip of the lower rotor blades. The axial additional velocity acting on the upper rotor at the radial position $r = 0$ at a distance $\bar{z} = \bar{z}_{ul}$ from the lower rotor plane is calculated with this model by

$$\frac{\bar{U}_{uz_{add}}}{\bar{U}_{lz|\bar{z}=0}} = 1 + \left(\frac{|\bar{z}|}{\sqrt{1+\bar{z}^2}} \right)^k sign(\bar{z}) \tag{19}$$

With $\bar{U}_{lz|\bar{z}=0}$ being the average induced axial velocity of the lower rotor.

$$\bar{U}_{lz|\bar{z}=0} = mean(\bar{w}_{lz}) \tag{20}$$

Following (Ref. 5) the value of the empirical parameter k is set to 0.5 as the upper influenced rotor resides above the lower rotor. The velocity $\bar{U}_{uz_{add}}$ is considered as an uniform additional axial inflow velocity influencing the entire upper rotor plane. The reason behind this approach is the expanded area of inflow drafted by the dashed lines in figure 3 originating from the momentum balance of the lower rotor.

Meanwhile the wake of the upper rotor will contract while traveling in the direction of the lower rotor. When the lower rotor has a radius $r_{l_{Tip}}$ greater than r_c as shown in figure 3 the inner portion $l1$ of the lower rotor with the radius r_c spanning the area $A_c = r_c^2\pi$ will be affected by an additional inflow velocity $\bar{U}_{l1_{add}}$ from the contracted wake while the outer portion $l2$ will experience no influence by the upper rotor.

The additional inflow originates from the velocity induced by the upper rotor $\bar{w}_u$ and is calculated in axial and azimuthal direction with a model by Giovanetti (Ref. 5) where $\bar{w}_{uz}$ and $\bar{w}_{u\theta}$ are the velocities induced by the upper rotor at its rotor plane.

$$\bar{U}_{l1z_{add}} = \bar{w}_{uz} \left(\frac{A}{A_c} \right) \tag{21}$$

$$\bar{U}_{l1\theta_{add}} = \bar{w}_{u\theta} \left(\frac{A}{A_c} \right)^{3/2} \tag{22}$$

The calculation of radius r_c is based on a simple generalized empirical model developed by Landgrebe (Ref. 14) for rotors in hover producing static thrust.

The model by Landgrebe divides the wake of a rotor in two distinct components as depicted in figure 4:

1. A tip vortex originating from the roll up of the vortex sheet at the tip of the rotor

2. A vortex sheet being shed from the trailing edge of the rotor blade over the whole radius.

Through experiments Landgrebe developed equations describing the axial and radial coordinates of those two wake structures based on the wake angle Ψ_w which is defined as the angle the rotor blade traveled since shedding the particular wake vortex element.

To calculate the radius of the contracted wake of the upper rotor when impacting the lower rotor only the tip vortex model of (Ref. 14) is used and modified to include the propagation of the wake vortex tube.

As the model was developed for a rotor in hover, the wake is assumed to experience a stretching effect caused by the inflow velocity U_z. This modification only considers the axial propagation distance $\bar{z}_S$ of the vortex tube as a lateral propagation is not assumed to change the wake contraction behavior but rather move the contracted wake in a lateral direction which is considered together with the oblique inflow considerations.

According to Landgrebe, a vortex element shed by the blade will travel downstream and inward, but not in azimuthal direction with the velocity induced by the rotor while the blade will continue rotating. As soon as the following blade has passed over the position of the element, the downwash produced by this blade will increase its axial velocity.

Thus, the normalized axial coordinate $\bar{z}_{Tip}$, defined with the positive direction pointing upward towards the inflow, is calculated differently when the following blade has traveled the angular distance between two blades $\Psi_w = \theta_b = \frac{2\pi}{N_b}$. This leads to the equations:

$$\bar{z}_T = \begin{cases} k_1 \Psi_w - \bar{z}_S \;\; \text{for } 0 \leq \Psi_w \leq \theta_b \\ \\ (\bar{z}_T)_{|\Psi_w = \theta_b} + k_2 \;\; (\Psi_w - \theta_b) - \bar{z}_S \;\; \text{for} \;\; \Psi_w \geq \theta_b \end{cases} \tag{23}$$

with constants $k1$ and $k2$ defined in (Ref. 14) as:

$$k1 = -0.25 \left(\frac{C_T}{\sigma} + 0.001 \Theta_{ulin} \right) \tag{24}$$

$$k2 = -\left(1.41 + 0.0141 \Theta_{ulin}\right) \sqrt{\frac{C_T}{2}} \tag{25}$$

where Θ_{ulin} is the linear blade twist calculated by

$$\Theta_{ulin} = \frac{\beta_{Tip} - \beta_{Hub}}{r_{Tip}} \tag{26}$$

For each case, the additional distance $\bar{z}_S$ will expand the wake depending on the inflow velocity. It is calculated using the age of the wake which is is dependent on the angular velocity of the rotor and the wake angle: $t = \Psi_w / \Omega$.

$$\bar{z}_S = \bar{U}_z \, \bar{t} = \bar{U}_z \, t \; \Omega = \bar{U}_z \Psi_w \tag{27}$$

As the axial distance $\bar{z}_T = \bar{z}_{ul}$ between the rotors is known and constant, equation (23) can be solved for the wake angle Ψ_w.

Depending on the angle traveled by the blades until the vortex element reached $\bar{z}_{ul}$ this leads to:

$$\Psi_w = \begin{cases} \dfrac{\bar{z}_T}{k_1 - \bar{U}_z} & \text{for } 0 \leq \Psi_w \leq \theta_b \\ \\ \dfrac{\bar{z}_T - (\bar{z}_T)_{\Psi_w = \theta_b} + k_2 \cdot \theta_b}{k_2 - \bar{U}_z} & \text{for } \Psi_w \geq \theta_b \end{cases} \tag{28}$$

This angle can be used in the formula of the radial tip coordinate given in (Ref. 14)

$$\bar{r}_c = r_{cmax} + (1 - r_{cmax}) \; e^{-\lambda \Psi_w} \tag{29}$$

With the parameter r_{cmax} being the maximum contraction radius found to be $r_{cmax} = 0.707$ by (Ref. 15) and (Ref. 3) and the parameter λ relating $\bar{r}$ and C_T is:

$$\lambda = 0.145 + 27 C_T \tag{30}$$

Subsequently the wake contraction radius $\bar{r}_c$ of the upper rotor at the position of the lower rotor can be calculated and used for the calculation of the additional inflow velocities.

This enables the application of the equations (7) and (8) to coaxial rotors.

The inflow velocities U_z and U_θ have to be modified to incorporate the additional velocities.

For the upper rotor $\bar{U}_{uz_{add}}$ is calculated using equation (19) and added to the axial inflow. The azimuthal inflow $\bar{U}_{u\theta}$ is not modified. The integration in radial direction is carried out for the whole blade $[r_{inner}, r_{outer}] = [r_{Hub}, r_{Tip}]$.

The calculation of the lower rotor has to be split at radius r_c. For the inner part $l1$, the additional velocities calculated in equations (21) and (22) have to be added to the axial and azimuthal inflow velocities. This part is integrated in radial direction from the hub to the contraction radius: $[r_{inner}, r_{outer}] = [r_{Hub}, r_c]$. The outer part $l2$ is calculated without any additional inflow velocities and is integrated from r_c to the blade tip: $[r_{inner}, r_{outer}] = [r_c, r_{Tip}]$.

This leads to the velocities $\bar{U}^{u/l}_{z_{total}}$ and $\bar{U}^{u/l}_{\theta_{total}}$ respectively depending on the rotor part calculated.

$$\bar{U}^{u/l}_{z_{total}} = \bar{U}^{u/l}_{z} + \bar{U}^{u/l}_{z_{add}} \tag{31}$$

$$\bar{U}^{u/l}_{\theta_{total}} = \bar{U}^{u/l}_{\theta} + \bar{U}^{u/l}_{\theta_{add}} \tag{32}$$

which can be written into the final equations for C_T and C_P by inserting the respective inflow velocities for the upper (u), lower inner ($l1$) or lower outer ($l2$) rotor.

$$C_T = \int_0^{2\pi} \int_{\bar{r}_{inner}}^{\bar{r}_{outer}} 4F \; (\bar{U}_{z_{total}} + \bar{w} \cos\phi) \; \bar{w} \cos\phi \; \bar{r} \\ - \sin\phi \; \frac{N_b \bar{c} c_d}{2\pi} \; \left(\bar{U}^2_{z_{total}} + (\bar{r} + \bar{U}_{\theta_{total}})^2 - \bar{w}^2 \right) \; d\bar{r} \tag{33}$$

$$C_P = \int_0^{2\pi} \int_{\bar{r}_{inner}}^{\bar{r}_{outer}} 4F \left(\bar{U}_{z_{total}} + \bar{w}\cos\phi\right) \bar{w}\sin\phi \; \bar{r} \; \left(\bar{r} + \bar{U}_{\theta_{total}}\right)$$

$$+\cos\phi \; \frac{N_b \bar{c} c_d}{2\pi} \; \left(\bar{U}^2_{z_{total}} + (\bar{r} + \bar{U}_{\theta_{total}})^2 - \bar{w}^2\right) \; (\bar{r} + \bar{U}_{\theta_{total}}) \, d\bar{r} \tag{34}$$

Similar to the single rotor above, the efficiency of the coaxial system has to be considered. As both rotors can take a different share of the total thrust e.g. when both rotors are tuned to balance the total torque $Q_{coax} = 0$ this has to be considered in the combined efficiency metric.

Leishman and Ananthan (Ref. 16) define this metric combining hovering condition and axial flight and thus also being valid for $U_\infty = 0$:

$$\eta_c = \frac{C_T \lambda_\infty + C_{Pu_{ideal}} + C_{Pl_{ideal}}}{C_T \lambda_\infty + C_{Pu} + C_{Pl}} \; . \tag{35}$$

With the tip speed ratio $\lambda_\infty = U_\infty / \Omega r_{Tip}$, the ideal power coefficients for both rotors are given by:

$$C_{Pu_{ideal}} = C_{Tu} \left(\frac{1}{2} \sqrt{\lambda_\infty^2 + 2C_{Tu}} - \frac{\lambda_\infty}{2} \right) \tag{36}$$

$$C_{Pl_{ideal}} = C_{Tl} \left(\frac{1}{2} \sqrt{\lambda_\infty^2 + 2C_{Tl}} - \frac{\lambda_\infty}{2} \right) \tag{37}$$

Using these equations and the iterative process described above enables the assessment of a coaxial rotor system. The numerical approach will be described below.

Numerical Modeling

The mathematical model described above has to be adapted to fit the numerical scheme present in the SARF environment (Ref. 7).

In this environment a rotor is defined in an object-oriented hierarchical class structure shown in figure 5 where all information on geometry, location in the UAV and environmental conditions is stored.

Multiple rotors on a UAV such as a coaxial rotor can be described separately to incorporate the application of the developed methods to the calculation of a wingtip pusher configuration.

Discretization and Integration Schemes As described above an arbitrary flight state will lead to an inflow that will vary in radial and azimuthal direction.

In azimuthal direction the rotor parameters are calculated at a variable number of azimuthal positions evenly distributed over one rotor revolution. The local varying flow conditions are considered at each position in a quasi static manner where

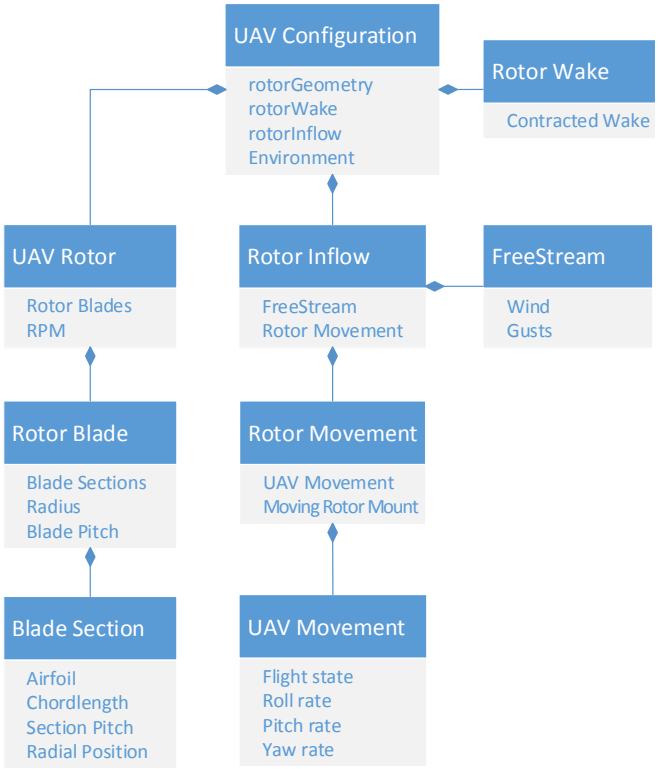

Fig. 5: Hierarchical class structure to represent the UAV

each state is considered static and no relaxation effects between different azimuthal position occur. The resulting forces can be resolved locally to calculate moments acting on the rotor hubs or can be integrated over the whole annulus.

Thrust and torque produced by the whole rotor are integrated first in azimuthal direction from $\theta = [0, 2\pi]$. These averaged values are then integrated in radial direction for the global performance values.

Inherent to the BEMT the discretization of the rotor in radial direction is done by placing multiple radial blade sections along the radius. The structure depicted in figure 5 permits the placement of an arbitrary amount of sections at arbitrary radial positions.

This flexibility is needed for additional sections that have to be placed in the lower rotor at the position where the wake of the upper rotor impinges on the lower rotor.

As shown in figure 6 the thrust- and other coefficients are calculated by trapezoidal integration between each section placed in radial direction. Due to the rapid change in axial and azimuthal inflow velocities at the radius r_c, the local thrust coefficient c_T will experience a step at this radius. By placing an additional section at $r = r_c$ the accuracy of the integrals of formulas (33) and (34) will be greatly increased as an integration boundary can only be considered at an existing section.

When including this additional section in the discretization all geometrical parameters will be interpolated between the two adjacent original sections. However, in case two different airfoil shapes with different airfoil coefficients c_l and c_d are present, a simple interpolation will not suffice. Instead the

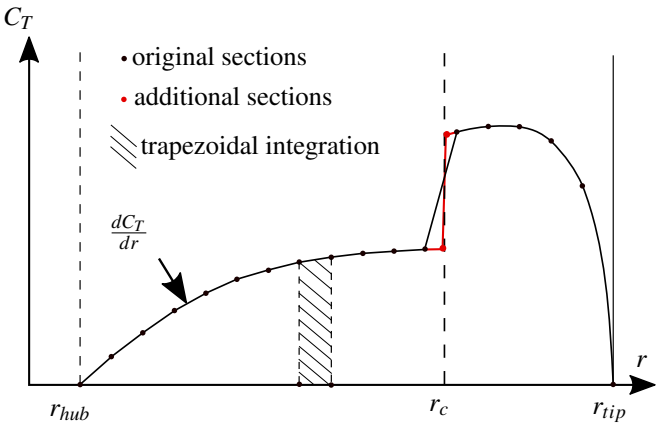

Fig. 6: Trend of dC_T/dr on the lower rotor of a coaxial rotor system, with inserted additional sections

airfoil coefficients of the new interpolated airfoil will be determined using an algorithm developed by Frank in (Ref. 17).

Iteration Scheme of the Coaxial System The iterative scheme shown in figure 2 is used for the individual rotors of the coaxial system. Because of the mutual influences another outer iteration loop has to be carried out.

After initializing both rotors the initial flow state of the upper rotor will be calculated first, according to figure 2 while not considering the additional inflow velocity induced by the lower rotor. With the results the wake contraction radius r_c of the upper rotor will be calculated at the position of the lower rotor $\bar{z}_{ul}$ using formula (29).

Using this radius, the additional inflow velocities $\bar{U}_{lz_{add}}$ and $\bar{U}_{l\theta_{add}}$ will be calculated and added to the nominal inflow acting on the lower rotor using equations (21) and (22). Here, the scheme depicted in figure 2 is executed for the inner and outer part separately. Once convergence on both parts is achieved the additional velocity $\bar{U}_{uz_{add}}$ is determined by formula (19) and the iteration for the upper rotor is started anew.

This process is repeated until all additional induced velocities converge at every section and azimuthal position. Then the performance values of the individual rotors and the coaxial system can be determined.

Application to Wingtip Pusher Propellers

The knowledge gained in the previous sections is now applied to another rotor configuration shown in figure 7 that experiences equivalent flows: When mounting a pusher propeller at the wingtip of a fixed-wing UAV the propeller operates in the slipstream of the separating vortex.

This tip vortex depicted in figure 8 starts at the leading edge of the wing with the span b and expands with further distance to the wing. It will consist of a vortex core with radius r_{core}, where the induced axial velocity will resemble rigid body rotation and an outer part where the induced velocity is dependent on the vortex strength Γ according to the Biot-Savart-Law.

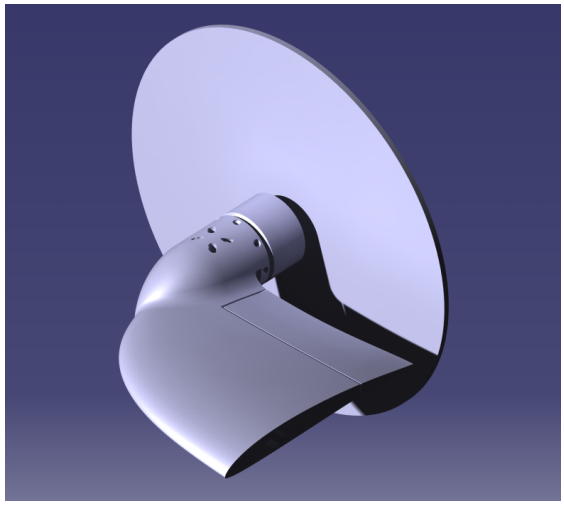

Fig. 7: Visualization of a wingtip mounted pusher propeller at a fixed-wing UAV (TUM-LLS, 2018)

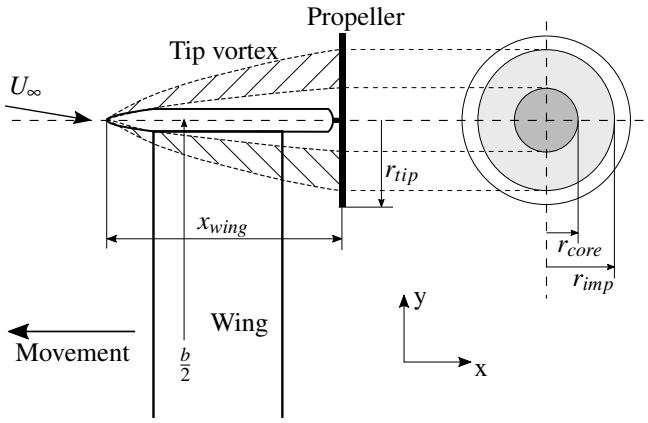

Fig. 8: Draft of a wingtip-mounted pusher propeller, with an inflow U_∞

As the distance between the propeller and the leading edge x_{wing} will be rather small, the vortex expansion will generally be less than the total propeller radius. When using a simple Biot-Savart model for the induced azimuthal velocity the influenced area expands infinitely. However it is also possible to define a limit of the influenced area which leads to an outer boundary r_{imp} where no influence is exerted for radii greater than r_{imp}. Figure 8 also shows an inclined flow U_∞ impacting the wing which can be experienced when the UAV is in yawed flight. This phenomenon impacts the wingtip vortex in a similar manner than an inclined inflow to a coaxial rotor system.

The system will induce an additional axial and azimuthal velocity on the part of the propeller disk which resides in its area of influence. Together these phenomena can be applied to the coaxial rotor model described above where the upper rotor is replaced by the wingtip vortex.

Using either the model described below or any other suitable method to determine the additional inflow velocities on the wingtip propeller $\bar{U}_{wtz_{add}}$ and $\bar{U}_{wt\theta_{add}}$, the total velocities $\bar{U}_{wtz_{total}}$ and $\bar{U}_{wt\theta_{total}}$ can be calculated. These are used in the

scheme shown in figure 2 for the lower rotors inner and outer area separated by r_{imp} to get the performance values with the equations (33) and (34).

The influence of the propeller on the wing is not considered here but can be assessed similarly to the influence exerted on the upper by the lower rotor of the coaxial system when using a more sophisticated model to calculate the vorticity on the wing.

Velocities Induced on Pusher Propeller To determine the velocities induced on the propeller, Prandtl's simple lifting line theory is used. Following the approach of Beguin (Ref. 18) and analogous to the discretization used for the rotor blades, the total lift L produced by the wing of a UAV is calculated by integrating the sectional lift $l(y)$:

$$L = \int_{-\frac{b}{2}}^{\frac{b}{2}} l(y)\, dy \tag{38}$$

The Kutta-Joukowski Theorem states that lift can only be produced by a bound vortex $\Gamma(y)$ on the wing. It is related to the lift distribution by:

$$\Gamma(y) = \frac{l(y)}{\rho U_\infty} \tag{39}$$

The local lift can be expressed by the lift coefficient c_l

$$l(y) = \frac{1}{2} c_l\, c(y) \rho U_\infty^2 \tag{40}$$

and this term substituted in equation (39) to relate the bound vorticity to the local lift coefficient:

$$\Gamma(y) = \frac{1}{2} c_l\, c(y) U_\infty \tag{41}$$

This bound vorticity can be used to calculate the influence on the propeller.

Wing Vortex Influence The additional velocities acting on the propeller $\bar{U}_{wtz_{add}}$ and $\bar{U}_{wt\theta_{add}}$ are calculated based on a model by Garmann and Visbal (Ref. 19).

The azimuthal component originating from the rotational vorticity is induced according to the vortex core model by Lamb-Oseen used by Bhagwat and Leishman (Ref. 20) inside the core radius r_{core} and decreases exponentially following equation 42 outside the core.

$$\bar{U}_{wt\theta_{add}}(r) = \frac{\Gamma}{2\pi r} \left[1 - \exp\left(-\frac{r^2}{r_{core}^2}\right)\right] \tag{42}$$

The core radius r_{core} of the vortex according to the core model is expanding while traveling downstream of the wing and is given at the location of the propeller x_{wing}:

$$r_{core} = \sqrt{r_{core0}^2 + 4\alpha\nu\frac{x_{wing}}{U_x}} \tag{43}$$

Here, α is the Oseen Parameter of the vortex core model and is fixed to $\alpha = 1.25643$. The initial vortex core radius is dependent on the geometry where the vortex originates and is set to the trailing edge thickness of the wing.

Knowing the azimuthal component it is possible to determine the axial component of the wingtip vortex.

$$\bar{U}_{wtz_{add}} = U_\infty + \Delta u \exp\left(-\frac{r^2}{r_{core}^2}\right) \tag{44}$$

The axial velocity deficit Δu is defined by Garmann and Visbal (Ref. 19) being proportional to the maximum azimuthal velocity $\max(\bar{U}_{wt\theta_{add}})$ using a swirl parameter q which is set to be greater than $\sqrt{2}$:

$$q \approx 1.567\, \frac{\max(\bar{U}_{wt\theta_{add}})}{\Delta u} \tag{45}$$

With this model being based on the Biot-Savart-Law there is no outer boundary r_{imp} limiting the influence of the wingtip vortex. However when a model is used where an outer influential boundary is present it can be easily incorporated as described above.

Computational Results and Validation

The results of the model are validated using the HR1 rotor which was examined by Harrington (Ref. 9). Although the HR1 is a full scale coaxial helicopter rotor it is used for validation as detailed measurement data as well as a detailed description of the geometry are publically available. It is also used by many other publications concerning coaxial rotors and thus is well suited to compare different methods. After determining the correctness of the proposed models the application to wingtip pusher propellers is shown by comparing the pusher performance to that of a propeller operating in undisturbed flow.

Coaxial Validation Leishman and Ananthan (Ref. 3) used the HR1 measurements to validate their BEMT model which does not consider azimuthal components of the induced velocity. This was done using the deviation of a free vortex analysis (FVA) as the original data collected by Harrington does not include sectional thrust and torque coefficient measurements. Leishman determined the correct calculation of the FVA by comparing the global thrust and torque measurements with the measured data by Harrington. As the data was in good agreement with the measurements, he compared the sectional values obtained by the FVA with his implementation of the BEMT. While the prediction of the BEMT for the thrust coefficient was only slightly under predicted, the torque coefficients were slightly more underestimated. As it is desired to validate the sectional values of the BEMT used here these results will be used for comparison rather than the original measured data by Harrington.

Harrington used two geometrically equal two bladed rotors for the measurements as shown in figure 9. They consisted of untwisted blades with linear taper and 4-digit NACA airfoils.

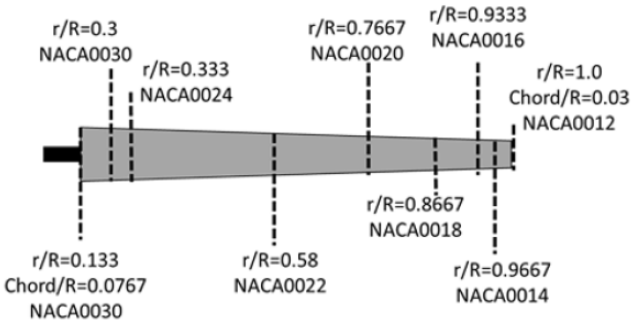

Fig. 9: Blade planform of Harrington Rotor 1 (Ref. 2)

Table 1: Geometric parameters of the Harrington Rotor 1 in hover

Parameter	**Value**
R_{Tip}/R_{Hub}	3.81m/0.507m
N_b	2
c	linear taper [0.0767;0.03]
z_{ul}	0.71m
V_{Tip}	152.4m/s
σ per rotor	0.027
Twist	none
Airfoils	4 digit NACA
Direction upper rotor	Clockwise
Direction lower rotor	Counter-clockwise

The detailed geometry is listed in table 1. The blades are mounted on a variable pitch hub and able to adjust their global pitch angle β_{global}

The operating conditions used by Leishman are characterized by both rotors operating at torque balance where the total torque coefficient $C_Q = C_{Qu} + C_{Ql}$ is zero. This is achieved with the upper rotor producing more thrust ($C_{Tu}/C_{Tl} = 1.25$) and both rotors operating at the tip speed indicated in table 1.

When replicating these operating conditions with the model described above the data can be compared. Figure 10 shows the thrust coefficient of the upper rotor over the radius.

The sectional positions of the calculation are marked with a cross starting at the rotor hub. At a radial position of $\bar{r} \approx 0.8$ one can clearly see two sections being closer together. This is due to the wake contraction radius r_c where two additional sections are added directly left and right of r_c as discussed in figure 6. Due to the implementation, the sections are also added to the upper rotor. Furthermore the data generated by Leishman is cut off at a radial position of $\bar{r} = 0.2$ whereas this model is calculated up to the rotor hub.

The trend is in very good agreement with the reference data. There are small deviations for the outermost sections which can be explained by a different tip loss behavior.

Subsequently figure 11 shows the thrust coefficient of the lower rotor. One can clearly see the jump where the wake of the upper rotor impinges on the lower rotor and the two sections placed at this position.

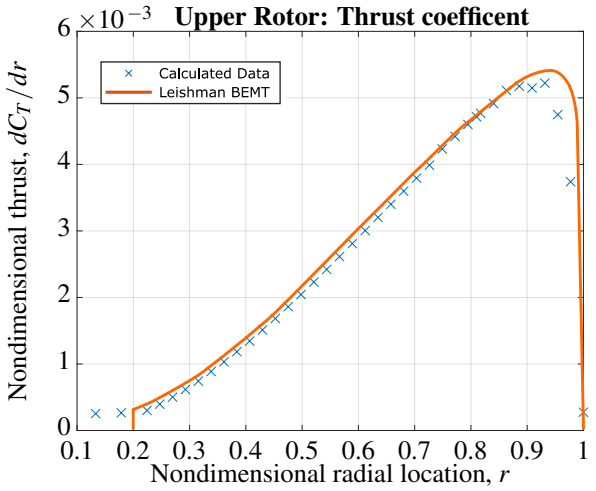

Fig. 10: Thrust dC_T/dr over r/R of the Upper HR1 in hover, comparison with data from Leishman

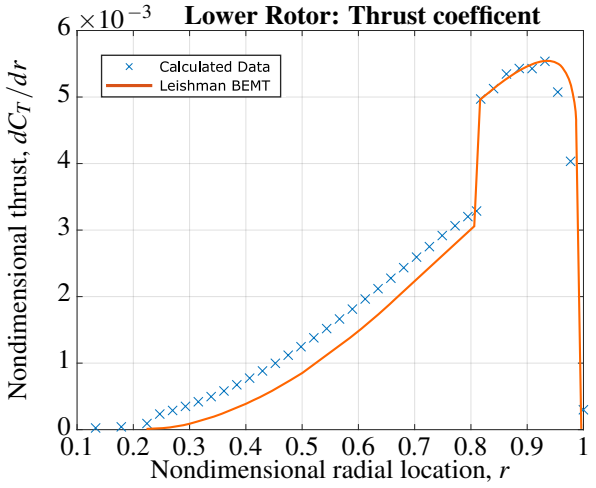

Fig. 11: Thrust dC_T/dr over r/R of the lower HR1 in hover, comparison with data from Leishman

The magnitude of the contraction radius r_c is determined and the adjacent sections are adjusted in every iteration. The progression of the radius, which can be seen in figure 12, is very stable and settles rather quickly. The converged result of $\bar{r}_c = 0.809$ has a difference of less than 1% to the value of $\bar{r}_c = 0.811$ determined by Leishman.

The overall trend of the lower thrust coefficient is also in good agreement with the data. The thrust coefficient is slightly overpredicted at the inner sections which can be explained by the additional consideration of azimuthal induced velocities

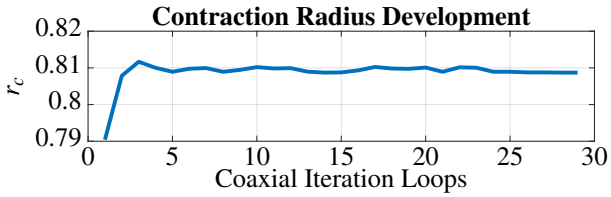

Fig. 12: Development of the Contraction Radius r_c with each iteration.

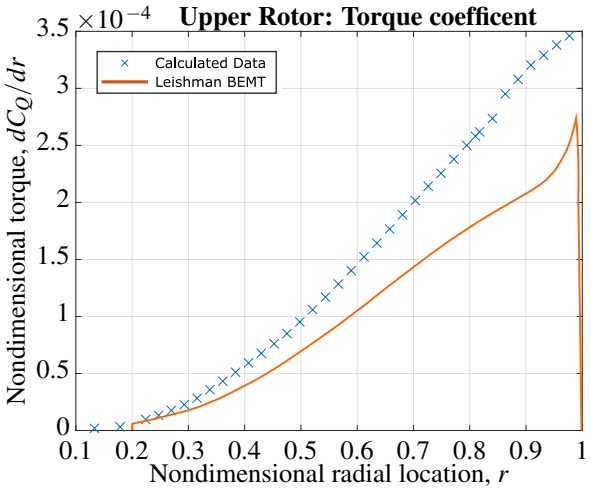

Fig. 13: Torque dC_Q/dr over r/R of the upper HR1 in hover, comparison with data from Leishman

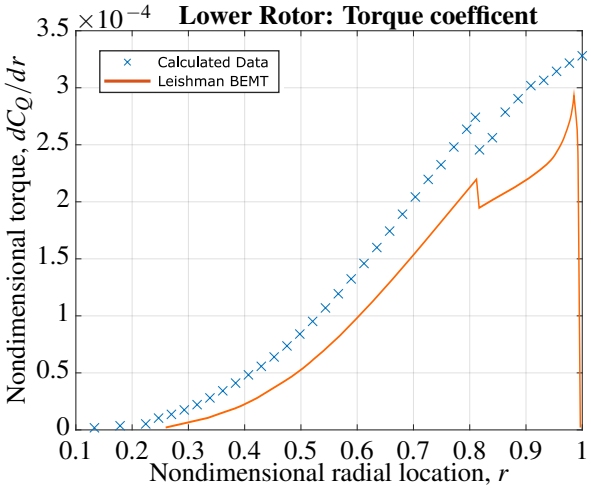

Fig. 14: Torque dC_Q/dr over r/R of the lower HR1 in hover, comparison with data from Leishman

which lowers the local inflow angle ϕ and thus increases the local AoA α. This will produce a higher thrust coefficient which can be seen here.

As the outer sections are not affected by the additional induced velocity there is no overprediction. The model rather experiences similar behavior to the upper rotor where a different consideration of the tip losses leads to small deviations.

The torque coefficient corresponding to the power consumption of the rotors is also considered. Figure 13 shows the torque coefficient of the upper rotor and figure 14 of the lower rotor. Due to the additional azimuthal velocity components the local inflow is tilted compared to the BEMT by Leishman. This increases the torque required to turn the rotor greatly.

As described in (Ref. 3) the reference data used here predicts less thrust than the FVA that was tuned to match the experimental results. The overestimation of the torque coefficient calculated here is compensating the underestimation residing in the underlying data.

Overall the data show a good agreement with the measurements and also show the effect of the additional azimuthal velocities.

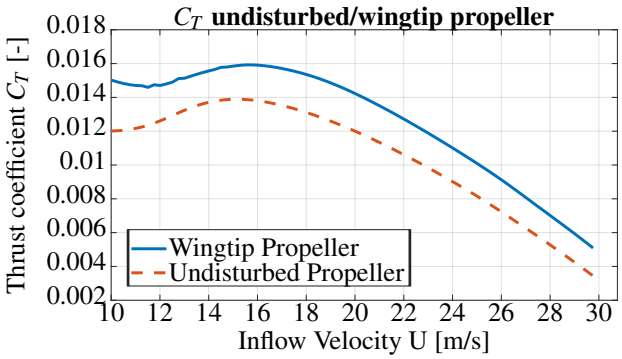

Fig. 15: Rotor thrust coefficient C_T over wingtip inflow velocity

Wingtip Propeller Performance As discussed above, when analyzing a pusher propeller operating behind the wingtip of a fixed wing the azimuthal velocities that are additionally affecting the rotor will reduce the inflow angle ϕ and increase the AoA α. This leads to a higher thrust generation compared to a propeller with an undisturbed inflow. However, as seen in figure 14 it will also greatly increase the required torque and thus the power consumption.

The usefulness of this effect depends entirely on the rest of the configuration and the propeller that is used and cannot be predicted here as the efficiency of a powertrain (ESC, motor and propeller) is not varying in a linear manner. Simply reducing the throttle setting will usually not result in an overall reduction of required energy. However, the wingtip effect can have other consequences.

In general, when designing a small eVTOL UAV it is often desired to operate in a certain regulatory environment which depends on the MTOW. This leads to a design goal where the MTOW is a fixed value that cannot be exceeded. Additionally, for any task except the transport of variable payloads the payload mass is also fixed which results in any residual mass possibly being invested in battery mass.

The pusher configuration will reduce the induced drag of the wing by acting against the vortex. This leads to a smaller thrust required. Additionally the higher thrust produced can lead to a smaller powertrain being sufficient for the design mission. Investing this mass reduction in more battery mass can deliver more energy than the increased energy consumption of the propeller compared to the undisturbed flow will use. In this case a wingtip pusher propeller is beneficial to the UAV design.

These considerations can also be seen in figure 15. For this calculation a 8x6 propeller with a diameter of 8 inch and a blade pitch of 6 inch is used while each blade is turned by an additional pitch of 10 degrees. As described above the model used for the wingtip vortex does not have an outer vortex boundary and the core radius is rather small, thus the whole annulus of the propeller is affected by the vortex with a radially decreasing induced velocity.

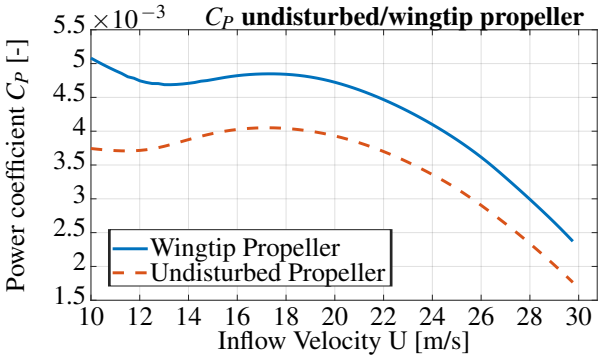

Fig. 16: Rotor Power coefficient C_P over wingtip inflow velocity

Figure 15 shows the thrust coefficient of an undisturbed propeller operating with free inflow as a dashed line. This data was calculated using the process described in figure 2 for a single rotor. The other line depicts the same propeller behind a wingtip with an impinging vortex.

The wingtip pusher propulsion system is operated at a constant $rpm = 7200$ for different cruise velocities. According to equation (39) the vortex strength is a function of the lift produced by the wing and decreases with an increasing incoming velocity. This can be seen as the thrust coefficient difference between the wingtip and the undisturbed propeller is decreasing with a faster inflow velocity.

The propeller exhibits a reduced C_T in the slow flying region as the pitch is quite high which results in a high AoA and subsequently stalled sections near the hub producing less thrust. The thrust coefficient increases with the inflow velocity while more sections are operated at optimal AoA. It can clearly be seen that the azimuthal velocity components caused by the wingtip vortex increase the local AoA and thus increase the thrust coefficient.

However the required torque is also higher than for the undisturbed inflow which is shown in figure 16. An increased AoA is leading to greater profile drag which increases the power coefficient C_P. However as stated above when the required thrust is fixed, the rotor can be operated at a lower rotational speed which redeems additional power.

Whether this process results in less power consumed by the propeller or the energy consumption staying constant depends on the propeller and the airfoils that are used. Figure 17 shows the relative efficiency difference $\Delta\eta$ in percent between the two operating states over the nominal operating rpm range at an exemplary inflow velocity of $U_x = 14\frac{m}{s}$:

$$\Delta\eta = \frac{\eta_{wt} - \eta_{free}}{\eta_{wt}} \quad [\%] \tag{46}$$

The propeller efficiencies are almost equal over a wide rpm range and also over a wide velocity range. When the rotational speed is reduced, there are no gains in required energy for this specific propeller. However the propeller operating behind the wingtip is still reducing the induced drag of the wing and thus reducing the overall thrust required by the UAV configuration

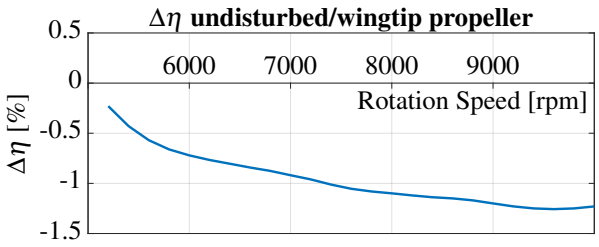

Fig. 17: Rotor efficiency difference $\Delta\eta$ over different rpm at $U_x = 14\frac{m}{s}$

which is beneficial for the endurance. A different propeller with different airfoils that are optimized for this flight state might also gain efficiency when operated behind a wingtip and thus further increase the endurance of the UAV.

CONCLUSIONS

The models developed show very promising results for the calculation of various flow states related to coaxial propulsion. The scheme devised for the single rotor (figure 2) can be the baseline calculation scheme for an individual rotor operating in hover, axial climb and cruise flight with prevalent oblique rotor inflow.

Because the impact of a vortex structure existing in the inflow can be calculated, various other rotor configurations can be assessed by applying this scheme to coaxial counter-rotating rotors or wingtip propulsion.

However, it is important to heed the constraints of the models which can also be addressed in future work on the topic. The interference between a rotor and its environment is only considered using the induced velocities. There is no calculation of a true wake vortex structure. Thus, there is also no consideration of wake turbulence.

As a result, the models proposed show only a limited applicability to coaxial co-rotating rotors like the hover rotors used for the *UBER Common Reference Model 001*. An extension of the calculations for this scenario would enable a detailed assessment of the advantages and disadvantages of the rotational direction.

With the calculations based on the BEMT the model uses a well established discretization basis for the geometry and show good agreement with the reference data.

This enables the fast calculation of a configuration for a given flight state without the need for manual geometry meshing activity. Thus this model can easily be incorporated in an optimization strategy with the aim to develop optimal rotor geometries for a given UAV and its mission.

Author Contact: Moritz Thiele moritz.thiele@tum.de – Martin Obster martinobster@gmx.de – Mirko Hornung mirko.hornung@tum.de

REFERENCES

[1]Jimmy C. Ho, Hyeonsoo Yeo, and Mahendra Bhagwat. Validation of Rotorcraft Comprehensive Analysis Perfor-

mance Predictions for Coaxial Rotors in Hover. *Journal of the American Helicopter Society*, 62(2):1–13, 2017.

[2]Natasha Barbely, Luke Novak, and Narayanan Komerath. A Study of Co-Axial Rotor Performance and Flow Field Characteristics. *AHS Technical Meeting on Aeromechanics*, 2016.

[3]J. Gordon Leishman and Shreyas Ananthan. An Optimum Coaxial Rotor System for Axial Flight. *Journal of the American Helicopter Society*, 53(4):366, 2008.

[4]Ramin Modarres and David A. Peters. Optimum Actuator-Disk Performance in Hover and Axial Flight by a Compact Momentum Theory with Swirl. *Journal of the American Helicopter Society*, 60(1):1–10, 2015.

[5]Eli B. Giovanetti and KennethC. Hall. Minimum Loss Load, Twist, and Chord Distributions for Coaxial Helicopters in Hover. *Journal of the American Helicopter Society*, 62(1):1–9, 2017.

[6]M. Thiele. *Entwicklung eines Programms zur Auslegung und Berechnung von instationär nicht planar angeströmten Rotoren*. Semesterthesis, Technical University Munich-TUM, München, 2015.

[7]M. Thiele. *Erweiterung und Validierung eines Rotortools mit Vorbereitung einer Konfigurationsstudie*. Masterthesis, Technical University Munich- TUM, München, 2016.

[8]Charles N. Adkins and Robert H. Liebeck. Design of optimum propellers. *Journal of Propulsion and Power*, 10(5):676–682, 1994.

[9]R. D. Harrington. Full-scale-tunnel investigation of the static-thrust performance of a coaxial helicopter rotor. (NACA-TN-2318), 1951.

[10]Richard C. Dingeldein. Wind Tunnel Studies of the performance of Multirotor Configurations. (NACA-TN-3236), 1954.

[11]K. W. McAlister, C. Tung, O. Rand, V. Khromov, and J. S. Wilson. Experimental and Numerical Study of a Model Coaxial Rotor. *Journal of the American Helicopter Society*, 62, 2006.

[12]J. Ost. *Parameterbasierte Modellierung von Rotor-Anstroemungszustaenden*. Bachelorsthesis, Technical University of Munich, Garching, 2017.

[13]A. Betz. Schraubenpropeller mit geringstem Energieverlust. Mit einem Zusatz von l. Prandtl. *Nachrichten von der Gesellschaft der Wissenschaften zu Göttingen, Mathematisch-Physikalische Klasse*, 1919:193–217, 1919.

[14]Anton J. Landgrebe. The Wake Geometry of a Hovering Helicopter Rotor and Its Influence on Rotor Performance. *Journal of the American Helicopter Society*, 17(4):3–15, 1972.

[15]Eli B. Giovanetti. *Optimal Aerodynamic Design of Conventional and Coaxial Helicopter Rotors in Hover and Forward Flight*. ProQuest Dissertations And Theses, Duke University Press, dissertation abstracts international, volume: 77-05(e), section: b.; 193 p. edition, 2015.

[16]J. Gordon Leishman and Shreyas Ananthan. Aerodynamic Optimization of a Coaxial Proprotor. *62th Annual Forum and Technology Display of the American Helicopter Society International*, page 64, 2006.

[17]M. Frank. *Geometriebasierte Abschätzung von unbekannten Profilbeiwerten*. Bachelors Thesis, Technical University of Munich, Garching, 2018.

[18]Benoit Beguin. *Development and analysis of an elasto-flexible morphing wing*. Dissertation, Technical University of Munich, München, 2014.

[19]D. J. Garmann and M. R. Visbal. Interactions of a streamwise-oriented vortex with a finite wing. *Journal of Fluid Mechanics*, 767:782–810, 2015.

[20]M. J. Bhagwat and J. G. Leishman. Generalized Viscous Vortex Model for Application to Free-Vortex Wake and Aeroacoustic Calculations. In Vertical Flight Society, editor, *58th Annual Forum and Technology Display of the American Helicopter Society International*, 2002.